Variational *R*-matrix calculations for singly and doubly excited singlet gerade channels in H_2

S. Bezzaouia,[1] M. Telmini,[1] and Ch. Jungen[2]
[1]*LSAMA Department of Physics, Faculty of Sciences of Tunis, University of Tunis El Manar, 2092 Tunis, Tunisia*
[2]*Laboratoire Aimé Cotton du CNRS, Université de Paris–Sud, 91405 Orsay, France*
(Received 12 January 2004; revised manuscript received 8 April 2004; published 30 July 2004)

Variational *ab initio R*-matrix theory is combined with generalized multichannel quantum defect theory, implemented in spheroidal coordinates, to calculate clamped-nuclei $^1\Sigma_g^+$, $^1\Pi_g$, and $^1\Delta_g^+$ electron-ion scattering phase shift matrices for H_2. The calculations cover the bound state region below H_2^+ $1\sigma_g$, the resonance region between H_2^+ $1\sigma_g$ and H_2^+ $1\sigma_u$, and they extend beyond the H_2^+ $1\sigma_u$ threshold. They span the range of internuclear distances $1 \leqslant R \leqslant 5$ a.u. The use of spheroidal instead of spherical coordinates allows a restricted partial wave expansion to be used, thus yielding a compact set of interaction parameters pertaining to the electron-ion scattering dynamics in H_2. The accuracy of our fixed-nuclei quantum defects is generally of the order of about 0.02. At the same time the quantum defect matrices obtained here exhibit a smooth behavior across the ionization thresholds and their elements also vary rather smoothly with internuclear distance. These results represent a step toward the goal of constructing a unfied theoretical description of ionization and dissociation fragmentation dynamics of H_2.

DOI: 10.1103/PhysRevA.70.012713 PACS number(s): 34.60.+z, 31.10.+z, 31.25.−v, 34.80.Kw

I. INTRODUCTION

In a recent paper [1] we described a new implementation of the variational *ab initio R*-matrix method and we presented calculations of the singlet *ungerade* excitation channels of H_2. These calculations gave quantum defect matrices both for the discrete and the continuum ranges in a single unified procedure, that are smooth functions of the total energy and the internuclear distance. This smooth behavior is desirable because of the physical insight it provides, and it is a prerequisite for a fully *ab initio* unified description of the photoionization and photodissociation of H_2 including the rotational and vibrational degrees of freedom, a goal which has not been attained yet.

In this paper we present analogous calculations for the singlet gerade channels of symmetry $^1\Sigma_g^+$, $^1\Pi_g$, and $^1\Delta_g$. The $^1\Sigma_g^+$ channels are generally thought to be the main contributors to the dissociative recombination process of the H_2^+ ion with an electron. Rotational-electronic coupling mixes them with the $^1\Pi_g$ and $^1\Delta_g$ symmetries, which therefore logically are calculated at the same time.

Quasiexact ($\approx 10^{-5}$ a.u.) *ab initio* quantum chemical potential energy curves are available for all these symmetries, but do not exceed the $n=4$ [2–4] or (in a few cases) the $n=5$ excitation level [5,6]. The positions and widths of core excited autoionization resonances have been calculated by various authors, and in particular the lowest $^1\Sigma_g^+$ resonance which mediates the dissociative recombination process has been studied in many papers. O'Malley [7] has apparently been the first, in 1969, to calculate quasistationary (i.e., resonant) $^1\Sigma_g^+$ potential curves for doubly excited H_2 using the Feshbach projection technique. A few years later Bottcher and Docken [8] used similar methods to calculate the autoionization widths in addition to the resonant curves. Takagi and Nakamura [9] expressed the two-electron problem in a scattering theoretical framework using spheroidal corrdinates and thus demonstrated the resonant behavior of the electron-ion scattering phase shifts near the resonance energies. The more recent larger-scale calculations were initiated by Collins and Schneider [10], Gubermann [11], and Tennyson, Noble and Salvini [12] who used the linear algebraic method, the Feshbach projection operator technique and the *R*-matrix approach, respectively, to treat core excited channels in H_2. Extensive tables of resonance positions and widths for the various symmetries and internuclear distances were published a few years ago by Tennyson [13] and Sánchez and Martin [14] who used the Wigner-Eisenbud *R*-matrix method [13] and the Feshbach formalism implemented with *B*-spline functions [14]. Shimamura, Noble, and Burke [15] have calculated some higher resonances which are given in neither of those compilations.

In the late 1980s it was recognized [16–18] that the excited state dynamics of H_2, particularly of $^1\Sigma_g^+$ symmetry and including nuclear motion, is best envisioned in terms of vibrational-coordinate dependent nondiagonal electronic quantum defect matrices. Thereby the doubly excited structures that produce the electronic autoionization resonances are explicitly introduced as core-excited (negative energy) scattering channels on the same footing as the channels associated with the ground state core. The nondiagonal quantum defect matrices used in Refs. [16–18] to treat the nuclear-electronic coupling in the excited singlet *gerade* levels of H_2 were derived *a posteriori* from the quantum chemical clamped-nuclei potential energy curves of Refs. [2–4], whereas it appears desirable to evaluate them directly in an *ab initio* scattering procedure. Greene and Yoo [19,20] have attempted this. Our calculations are similar to Refs. [19] and [20] in many ways, but they are not limited to the $^1\Sigma_g^+$ symmetry and in addition our aim is to remove the main shortcoming of the work of Refs. [19] and [20], by producing quantum defect matrices that vary much more smoothly with energy and internuclear distance.

While the states and resonances calculated in the present work have been described theoretically before, the present paper provides a unification of the earlier work. The simul-

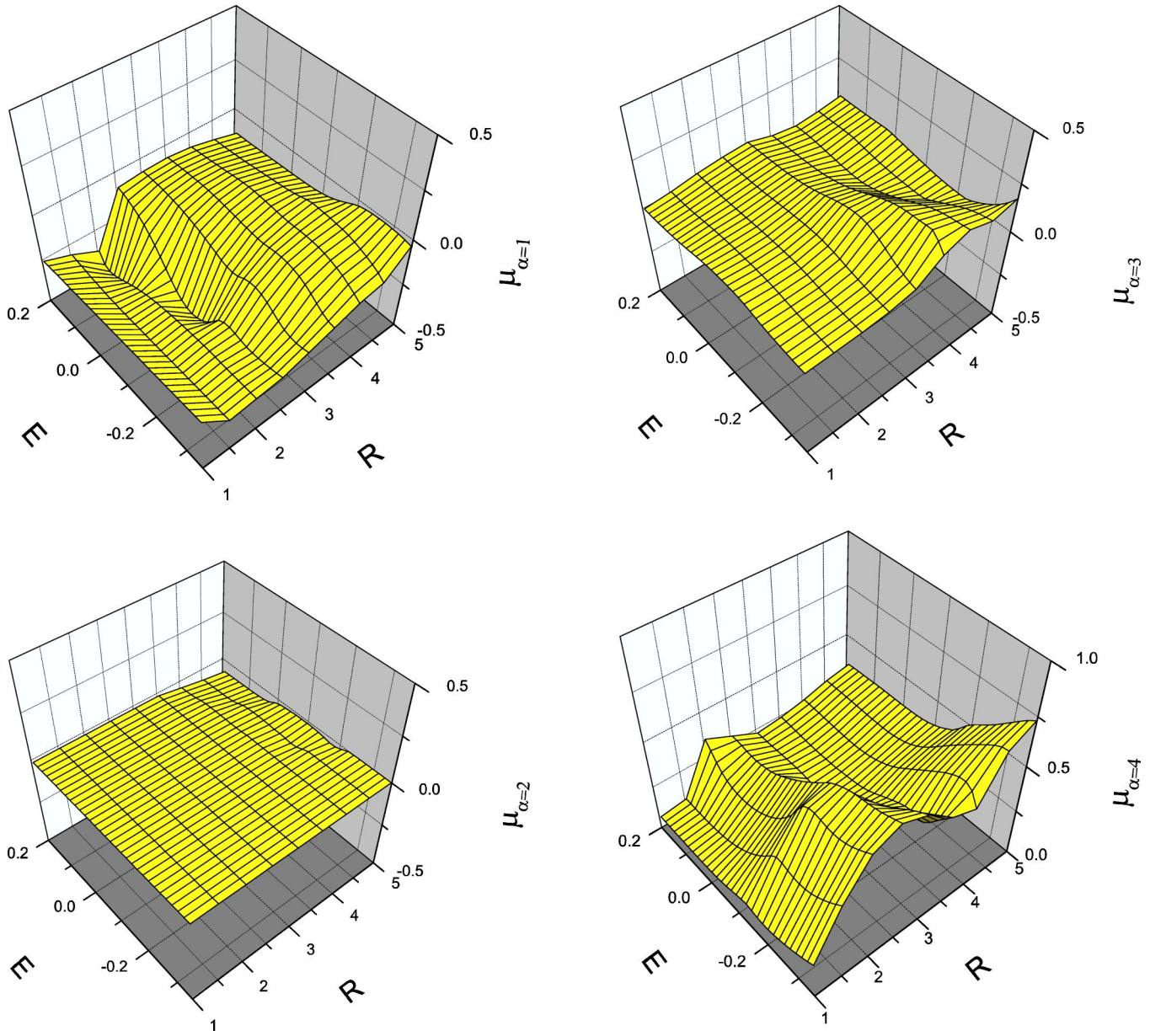

FIG. 1. *Ab initio* spheroidal eigenquantum defects μ_α for ${}^1\Sigma_g^+$ symmetry as functions of internuclear distance R (in atomic units) and energy E (in rydbergs). The zero of energy corresponds to the H_2^+ $1\tilde{s}\sigma$ threshold: (a) $\alpha=1$, (b) $\alpha=2$, (c) $\alpha=3$, and (d) $\alpha=4$. Note the different origin of the quantum defect scale employed for $\alpha=4$.

taneous *ab initio* calculation of bound as well as scattering states in a multichannel quantum defects framework yields a global picture of the electron-ion scattering dynamics which has not been available before and which is visualized by the quantum defect representations of Fig. 1. The resulting R- and E-dependent quantum defect matrix elements are intended for future use in dynamical scattering and bound state calculations including the nuclear degrees of freedom.

II. THEORY

The variational R-matrix approach employed here has been discussed in detail in Ref. [1]. Briefly, we use spheroidal coordinates ξ, η, ϕ and expand the two-electron wavefunction in terms of properly symmetrized products of H_2^+ one-electron orbitals. A configuration interaction treatment is set up in a finite volume $\xi \leqslant \xi_0$ and yields variational wavefunctions that have stationary logarithmic derivatives with respect to the spheroidal radial coordinate. Continuation of the wave function and its derivative beyond the finite R-matrix volume directly yields the desired reaction matrices $\mathbf{K}$ or equivalent quantum defect matrices μ.

The use of generalized quantum defect theory allows this continuation to be achieved in the framework of a unified formalism for the discrete region, the resonance region and the electronic continuum. As in the preceding paper [1] we denote the H_2^+ spheroidal one-electron wavefunctions in the finite volume by $n\tilde{l}\lambda$, and the corresponding channel func-

tions outside it by $\epsilon\tilde{l}\lambda$. Here $\tilde{l}$ is the spheroidal analog of the spherical orbital angular momentum l, and λ is the quantum number associated with the projection of the orbital angular momentum on the internuclear axis. $n-\tilde{l}-1$ is the number of radial nodes occurring inside the finite volume, while ϵ is the (negative or positive) one-electron channel energy. Thus, with the *R*-matrix radius chosen appropriately large, the two lowest spheroidal orbitals $1\tilde{s}\sigma$ and $2\tilde{p}\sigma$ H_2^+ are exponentially small on the reaction zone boundary ξ_0 and are identical with the $1\sigma_g$ or $1\sigma_u$ quantum chemical orbitals.

In our calculations we include the following two electron channel functions associated with the ground state core: $1\tilde{s}\sigma\epsilon\tilde{s}\sigma$ and $1\tilde{s}\sigma\epsilon\tilde{d}\lambda$ with $\lambda=0-2$. The core-excited channels included are $2\tilde{p}\sigma\epsilon\tilde{p}\lambda$ with $\lambda=0$ and 1, and $2\tilde{p}\sigma\epsilon\tilde{f}\lambda$ with $\lambda=0-2$. Explicit inclusion of these core-excited channels allows the electron-ion scattering resonances below the $2\tilde{p}\sigma$ excited state of H_2^+ to be removed from the quantum defect matrices; these resonances then reappear when asymptotic bound state boundary conditions are applied to the closed portion of the electron wavefunction. Assuming that only one electron effectively escapes from the core, it is reasonable to expect that the singly and doubly excited channel functions listed above describe the system outside the reaction volume adequately for energies up to and beyond the $2\tilde{p}\sigma$ H_2^+ ionization threshold. For yet higher energies higher core-excited channels would have to be included.

Inside the core region a much larger discrete basis of two-electron functions must be set up. We use a basis of typically about 200 antisymmetrized products of one-electron wavefunctions of the type $n\tilde{l}\lambda n'\tilde{l}'\lambda'$, where $1\leqslant n,\ n'\leqslant 10, 0\leqslant\tilde{l},\tilde{l}'\leqslant 3$, and where λ and λ' are chosen in accordance with the total symmetry $\Lambda=\lambda+\lambda'$, $^1\Sigma_g^+$, $^1\Pi_g$, or $^1\Delta_g$. Two types of such two-electron basis functions are actually used simultaneously in the computations, namely those which vanish at $\xi=\xi_0$ (and are referred to as closed-type functions), and those whose derivatives with respect to ξ vanish at $\xi=\xi_0$ (so-called open-type basis functions). The former constitute about 95% of the whole basis. The latter are added in order to provide the connection with the asymptotic channel functions discussed above. As in the previous paper [1] two open-type basis functions inside the reaction volume are included in the calculation for each channel taken into account asymptotically. Their energies are chosen close to the total energy E considered. As shown previously, this choice guarantees that the correct number of nontrivial solutions, corresponding to the number of asymptotic channels, is obtained in the *R*-matrix procedure.

The truncation of the basis sets to $\tilde{l}\leqslant 3$ both within and outside the reaction region may appear too drastic to be realistic. However, each spheroidal partial wave is itself a linear combination of a range of spherical waves, which is the larger the smaller the value of the radial coordinate. The use of spheroidal basic functions therefore amounts to a prediagonalization of the one-electron Hamiltonian and therefore greatly reduces the size of the problem.

The criteria determining the choice of the reaction volume have been discussed in Ref. [1]. In the present calculations ξ_0 has been taken as $\xi_0=15/R+1$ (where R is the internuclear distance in atomic units), i.e., somewhat larger than in the previous paper [1], and no polarization terms have been added to the potential in the external zone. The variational procedure yields the reaction matrix $\mathbf{K}(E,R)$ in nondiagonal form on the arbitrary $R-$ and $E-$ mesh chosen for the calculation. For the purposes of compact visualization we shall in the following use the eigenquantum defects μ_α which are defined in terms of $\mathbf{K}$ by the relation

$$\mu_\alpha(E,R)=\frac{1}{\pi}\tan^{-1}\sum_{kk'}U_{\alpha k}^{-1}K_{kk'}U_{k'\alpha}, \tag{1}$$

where the columns of $\mathbf{U}$ are the eigenvectors of $\mathbf{K}(E,R)$.

The clamped-nuclei bound states below the H_2^+ $1\tilde{s}\sigma$ threshold are obtained by generalized quantum defect theory as the solutions of the MQDT secular equation [21,23]

$$\det\left|\tan\beta_k(\epsilon_k)\delta_{kk'}+K_{kk'}(E)\right|=0, \tag{2}$$

which is solved separately for each R-value. β_k is the accumulated phase of the external electron in channel k, characterized by the channel energy $\epsilon_k=E-E_c^{(k)}$ where $E_c^{(k)}$ is the core energy. Note that for a one center Coulombic problem the quantity $\beta_k/\pi+\ell$ reduces to the familiar Rydberg effective principal quantum number $\nu_k=(-\epsilon_k)^{-1/2}$. The accumulated phase measures the number of half wavelengths of the electron wavefunction in the potential of the two partially screened nuclei. Equivalently, the integer part of β_k minus 1 gives the number of nodes of the radial part of the wavefunction. β_k is evaluated numerically by use of the procedures described in Ref. [24]. It is a smoothly increasing function of the channel energy as illustrated for example by Fig. 3 of Ref. [1].

Once β and $\mathbf{K}$ are known, Eq. (2) yields the full spectrum of eigenvalues $E_n(R)$ from $n=2$ to arbitrarily high n values. Owing to their smooth behavior β and $\mathbf{K}$ need be calculated only on a relatively coarse grid of energies, and interpolation procedures may be used to obtain them for arbitrary E values. The resulting eigenvalues $E_n(R)$ are equivalent to the molecular potential energies $U_n(R)$ once the proton-proton repulsion term $+2/R$ (in Rydbergs) is added. R-dependent effective principal quantum numbers $\nu_n(R)$ (not to be confused with the Coulombic accumulated phase mentioned above) are defined as

$$\nu_n(R)=\frac{1}{\sqrt{U^+(R)-U_n(R)}}, \tag{3}$$

where $U^+(R)$ is the energy (again in Rydbergs) of the H_2^+ $1\tilde{s}\sigma$ ground state. The quantity $\mu_n(R)=n-\nu_n(R)$ is the effective one-center Coulombic electronic quantum defect which, multiplied by π, gives the corresponding effective one-center Coulombic electron phase shift in the bound state n.

In the continuum above the $2\tilde{p}\sigma$ H_2^+ threshold inelastic scattering processes occur. Equation (2) must now be replaced [21,23] by

$$\det|\tan[-\pi\tau_\rho(E)]\delta_{kk'} + K_{kk'}(E)| = 0 \qquad (4)$$

for each energy, where $\pi\tau_\rho(E)$ ($\rho=1,\ldots,N_0$) are the eigenphases of the continuum channel interaction for a given energy E and N_0 is the number of open channels. Note, the different role of the accumulated phase β_k in Eq. (2) and of the eigenphase $\pi\tau_\rho$ in Eq. (4). The former is a quantity which is defined at the given energy ϵ_k for each channel k, and hence for every total energy E, irrespective of the presence of a core, in terms of the potential seen by the escaping electron outside the reaction zone. With β_k given, Eq. (2) can be satisfied only for a discrete set of total energies E_n or equivalently $U_n(R)=E_n(R)+2/R$. On the other hand, the set of eigenphases $\pi\tau_\rho$ actually *result* from solving Eq. (4). As Eq. (4) indicates, the quantities tan $\pi\tau_\rho$ coincide in fact with the eigenvalues tan $\pi\mu_\alpha$ of the reaction matrix **K** when all channels included are open, and as such are defined for every energy E.

When we consider resonances occuring in the continuum between the $1\tilde{s}\sigma$ and $2\tilde{p}\sigma$ H_2^+ thresholds, we must combine Eqs. (2) and (4) by using lines according to Eq. (2) for the closed channels associated with the $2\tilde{p}\sigma$ H_2^+ state, and lines according to Eq. (4) for the open channels associated with the $1\tilde{s}\sigma$ H_2^+state [21–23]. The presence of closed channels associated with H_2^+ $2\tilde{p}\sigma$ then leads to a resonant behavior of the eigenphases $\pi\tau_\rho(E)$ [21–23]. The derivative with respect to the energy of the eigenphase sum corresponds to the spectral density of states. A plot of this quantity versus the energy E yields a Breit-Wigner-type peak for each isolated resonance, from which the position $E_n^{(\mathrm{res})}$ and the width $\Gamma_n^{(\mathrm{res})}$ can be derived. Each resonance energy $E_n^{(\mathrm{res})}(R)$ in turn can be used to derive a resonance potential energy curve $U_n^{(\mathrm{res})}(R)=E_n^{(\mathrm{res})}(R)+2/R$ as well as the corresponding effective principal quantum number $\nu_n^{(\mathrm{res})}$ by means of Eq. (3), where $U^+(R)$ now is the potential energy of the H_2^+ $2\tilde{p}\sigma$ state. When pairs or clusters of resonances overlap, their resonance positions and widths are no longer well defined although, of course, Eqs. (2) and (4) remain perfectly valid.

III. RESULTS

A. $^1\Sigma_g^+$ symmetry: Potential energy curves

Figures 1(a)–1(d) are three-dimensional plots of the eigenchannel quantum defects for $^1\Sigma_g^+$ symmetry which we obtain as functions of the energy and the internuclear distance. It may be seen that while all of these quantum defect surfaces are globally smooth, two of them ($\alpha=2$ and 3) depend little on R and E and are close to zero for most of the (R,E) range shown. The two other eigenquantum defects μ_α exhibit a significant evolution with R, but depend relatively little on the energy, particularly for $R>2$. Inspection of the eigenvectors $U_{i\alpha}$ (not shown) indicates that the eigenchannels $\alpha=1,3$, and 4 are mixtures of the channels $1\tilde{s}\sigma\epsilon\tilde{s}\sigma$, $1\tilde{s}\sigma\epsilon\tilde{d}\sigma$, and $2\tilde{p}\sigma\epsilon\tilde{p}\sigma$, while $\alpha=2$ corresponds approximately to the $2\tilde{p}\sigma\epsilon\tilde{f}\sigma$ core excited channel. This latter involves a nearly nonpenetrating outer electron which participates only slightly in the channel interactions in the E and R ranges considered here.

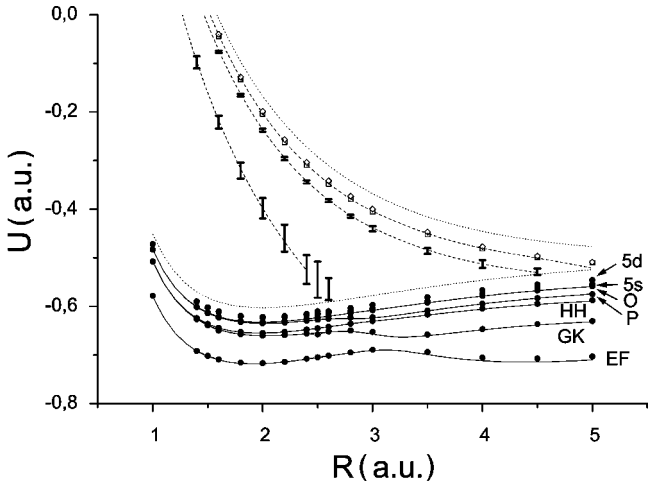

FIG. 2. Potential energy curves and resonances for $^1\Sigma_g^+$ symmetry (atomic units). Solid lines: quantum chemical *ab initio* results from Ref. [2] for the *EF*, *GK*, *HH*, *P*, and *O* states. Dashed lines, *ab initio* resonance positions from Ref. [13]; dotted lines, H_2^+ $1\tilde{s}\sigma$ and $2\tilde{p}\sigma$ thresholds; dots, present bound state calculations; bars, present positions and widths of the $(2\tilde{p}\sigma)^2$ and $2\tilde{p}\sigma 3\tilde{p}\sigma$ resonances;. squares and diamonds, present $2\tilde{p}\sigma 4\tilde{p}\sigma$ and $2\tilde{p}\sigma 4\tilde{f}\sigma$ resonance positions.

In order to test the accuracy of the *ab initio* scattering information thus obtained, we shall now use the data depicted in Fig. 1 to calculate known bound and resonance states of $^1\Sigma_g^+$ symmetry. Use of Eq. (2) with suitable interpolation of the $\mu_\alpha(E)$ of Eq. (1) [or equivalently of $\mu_{ij}(E)=\pi^{-1}\tan^{-1}K_{ij}(E)$] for each R yields the potential energy curves for the seven lowest $^1\Sigma_g^+$ excited states illustrated in Fig. 2 (dots). Figure 2 also depicts the quasiexact quantum chemical *ab initio* curves from Ref. [2] (full lines). Table I lists the effective principal quantum numbers $\nu_n(R)$ evaluated with Eq. (3) derived from our R-matrix work. They are compared in Fig. 3 with the corresponding data derived from the quantum-chemical potential energy curves from Ref. [2] for $n=2-4$. Figure 3 displays the differences $\Delta\nu_n=\nu_{ab\ initio}-\nu_{R-\mathrm{matrix}}$ as functions of R for the various states n. The error bars on the right indicate the mean value of $\Delta\nu_n$ for each state as well as its scatter. The energy deviation, in cm^{-1}, corresponding to the mean value of $\Delta\nu_n$ is also given. The deviations of our present effective principal quantum numbers from the corresponding quantum-chemical values amount to $|\Delta\nu_n|\approx 0.02$ in the average, or less, and the largest deviations are seen to occur at large R and, for some of the states near $R\approx 3$ a.u. where the $(2\tilde{p}\sigma)^2$ core excited state crosses the singly excited Rydberg manifold. The deviations are systematically negative, as should be expected because our variational calculations are not as sophisticated in terms of the basis sets used and therefore are not as well converged as the quantum-chemical *ab initio* calculations.

This agreement is similar to what we obtained previously for the $^1\Sigma_u^+$ and $^1\Pi_u$ symmetries [1]. Remembering that the effective principal quantum number *modulo 1* is to within a factor $-\pi$ equivalent to the effective Coulombic electron phase shift, we see that our calculations reproduce this quantity correctly to about 2%. As the focus of the present work

TABLE I. Clamped nuclei effective Rydberg principal quantum numbers $\nu_n(R)$[a] for bound $^1\Sigma_g^+$ states of H_2. The orbital designations $nl\lambda$ are valid for small R only.

R	$2s\sigma EF$	$3d\sigma GK$	$3d\sigma HH$	$4d\sigma P$	$4s\sigma O$	$5d\sigma$	$5s\sigma$
1.0	1.988	2.990	2.996	3.990	3.993	4.992	5.006
1.4	2.028	2.976	3.040	3.975	4.043	4.974	5.044
1.5	2.074	2.974	3.052	3.973	4.054	4.972	5.055
1.6	2.056	2.961	3.065	3.964	4.056	4.969	5.066
1.8	2.081	2.962	3.083	3.985	4.085	4.956	5.086
2.0	2.093	2.948	3.101	3.944	4.103	4.943	5.104
2.2	2.101	2.938	3.116	3.924	4.118	4.920	5.119
2.4	2.120	2.905	3.127	3.890	4.129	4.890	5.130
2.5	2.124	2.875	3.130	3.856	4.132	4.833	5.133
2.6	2.126	2.869	3.132	3.810	4.133	4.766	5.133
2.8	2.128	2.769	3.124	3.596	4.119	4.476	5.115
3.0	2.116	2.543	3.086	3.335	4.071	4.270	5.063
3.5	1.940	2.268	2.982	3.230	3.980	4.218	4.980
4.0	1.773	2.231	2.926	3.216	3.929	4.202	4.929
4.5	1.698	2.206	2.874	3.192	3.880	4.160	4.881
5.0	1.672	2.175	2.821	3.151	3.827	4.069	4.827

[a]Equation (3).

is basically on wavefunction properties, in particular phases, rather than on energies, we consider this agreement satisfactory. For $n=5$ (sixth and seventh excited states) no quantum-chemical curves are available in the literature. (These states have been calculated in Ref. [5] but are presented there only in graphical form.) We therefore compare with the *R*-matrix computations of Yoo and Greene [19,20] which can be seen to be equivalent to ours. The two *R*-matrix calculations thus give equivalent results, although it must be realized that the quantum defects themselves are very different (cf. the illustrations of eigenquantum defects given in Ref. [19]). We have previously encountered a similar situation for the $^1\Sigma_u^+$ symmetry, where our smooth quantum defect matrices gave potential energies quite close to those obtained by Yoo and Greene with their strongly *R*- and *E*-dependent quantum defects.

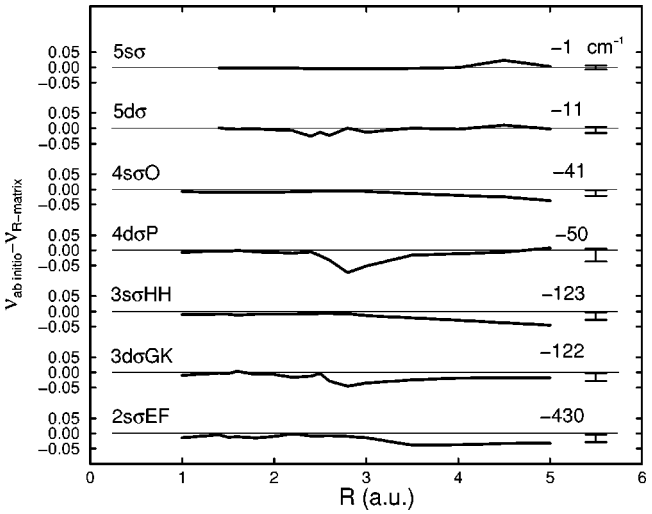

FIG. 3. Deviations $\Delta\nu_n=\nu_{ab\ initio}-\nu_{R\text{-matrix}}$ as functions of R for the bound $1-7$ $^1\Sigma_g^+$ states. ν_n is evaluated with Eq. (3). The *ab initio* data are from Ref. [2] except for $n=5$ (states 6 and 7) where we compare with the *R*-matrix calculations of Ref. [20]. The error bars on the right give the mean value and scatter of the deviations for each state. The numbers are the corresponding mean energy deviations in cm^{-1}.

B. $^1\Sigma_g^+$ symmetry: Resonances

Figure 2 also displays the positions of the $^1\Sigma_g^+$ resonances above the $1\tilde{s}\sigma$ threshold and, for the broad $(2\tilde{p}\sigma)^2$ and $2\tilde{p}\sigma 3\tilde{p}\sigma$ lowest resonances, the resonance widths. Notice how the width of the lowest resonance shown for $R\leqslant 2.6$ in Fig. 2 extrapolates visually smoothly to the avoided crossings seen in the discrete range for $R>2.6$. Table II contains our calculated $\nu_n(R)$ values for these and a few higher resonances. Figure 4 is a $\Delta\nu_n(R)$ plot analogous to Fig. 3, which gives the effective principal quantum number differences between the positions for the three lowest resonances $2\tilde{p}\sigma n\tilde{p}\sigma$ $(n=2-4)$ obtained here, and those given in the recent compilation of Tennyson [13]. *ab initio* here thus refers to Wigner-Eisenbud *R*-matrix calculations [13], in which three ion core states were included (rather than two as here), and where the scattering eigenphases including the resonance effects were obtained directly in the variational calculation (rather than in a separate MQDT step as here). We note in passing that the resonance parameters given by Sánchez and Martin [14] on the whole agree well with those of Ref. [13] (except for $R<1.5$ a.u., cf. Ref. [14], and for $\tilde{f}$-type resonances, see below). We will cite them therefore in detail only in a few particular instances. The deviations $\Delta\nu_n(R)$ of Fig. 4 are of the same order of magnitude as those shown in Fig. 3

TABLE II. Clamped nuclei energies and effective Rydberg principal quantum numbers for core excited $2\tilde{p}\sigma n\tilde{l}\sigma\ ^1\Sigma_g^+$ resonances of H_2. The orbital designations $nl\lambda$ are valid for small R only.

	$2\tilde{p}\sigma$		$3\tilde{p}\sigma$		$4\tilde{p}\sigma$		$4\tilde{f}\sigma$	
R	E[a]	ν[b]	E	ν	E	ν	E	ν
1.0	1.3802	1.594	1.6448	2.783	1.7047	3.800	1.7115	4.002
1.2	1.1446	1.576	1.4164	2.763	1.4776	3.785	1.4849	4.000
1.4	0.9350	1.563	1.2114	2.743	1.2734	3.753	1.2817	3.994
1.5	0.8306	1.541	1.1177	2.732	1.1804	3.746	1.1891	4.000
1.6	0.7400	1.535	1.0296	2.721	1.0930	3.736	1.1021	3.998
1.8	0.5597	1.495	0.8696	2.696	0.9346	3.712	0.9445	3.995
2.0	0.4091	1.473	0.7304	2.675	0.7969	3.693	0.8076	3.997
2.2	0.2825	1.460	0.6098	2.655	0.6777	3.678	0.6890	3.995
2.4	0.1445	1.407	0.5057	2.639	0.5747	3.663	0.5865	3.991
2.6	0.0531	1.403	0.4165	2.631	0.4863	3.659	0.4982	3.992
2.8			0.3401	2.629	0.4101	3.659	0.4220	3.991
3.0			0.2747	2.633	0.3444	3.663	0.3561	3.989
3.5			0.1500	2.666	0.2172	3.690	0.2278	3.986
4.0			0.0663	2.724	0.1296	3.740	0.1381	3.987
4.5			0.0105	2.798	0.0692	3.806	0.0753	3.987
5.0					0.0280	3.885	0.0315	3.990

[a]Energy in rydbergs above the $1\tilde{s}\sigma$ threshold.
[b]Equation (3).

for the bound states, but by contrast with Fig. 3 their mean values are not systematically negative.

The calculated widths of the $2\tilde{p}\sigma n\tilde{p}\sigma(n=2-4)$ resonances are given in Table III and illustrated by Fig. 5(a) (circles) and compared with those evaluated by Tennyson [13] (full lines). The two sets of widths agree well. The apparent decrease of the $(2\tilde{p}\sigma)^2$ resonance for $R=2.6$ a.u. in our calculation is related to the fact that this resonance is very close to the $1\tilde{s}\sigma$ threshold and in fact straddles it (i.e., part of the resonance has actually passed into the discrete range). This decrease is not substantiated by the work of Sánchez and Martin [14] who used the Fermi golden rule and give a width of 0.146 Ry for this resonance at $R=2.705$ a.u. Note, however, that in such a circumstance the concept of a Lorentzian width starts breaking down anyway and, as pointed out in Sec. II, only the energy dependence of the continuum phases remains meaningful. We stress again that our raw quantum defect matrices are smooth, up to and beyond, the threshold, and yet, by means of Eqs. (2) and (4), embody all the information concerning the inelastic scattering process involving a $\tilde{p}\sigma$ or $\tilde{f}\sigma$ outer electron with arbitrary principal quantum number.

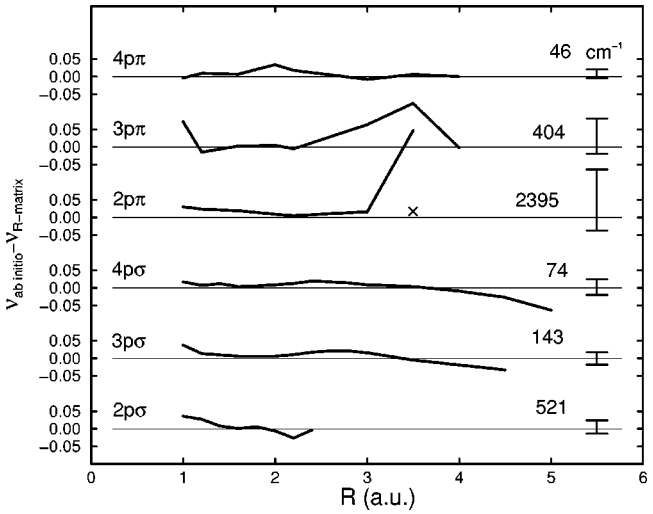

FIG. 4. Deviations $\Delta\nu_n=\nu_{ab\ initio}-\nu_{R\text{-matrix}}$ as functions of R for $^1\Sigma_g^+$ and $^1\Pi_g$ $2\tilde{p}\sigma n\tilde{p}\lambda$ resonance positions. ν_n is evaluated with Eq. (3). The *ab initio* reference data are R-matrix results from Ref. [13]. The cross $(2\tilde{p}\pi, R=3.5)$ is derived from Ref. [14]. The error bars have the same meaning as in Fig. 3. The numbers on the right-hand side give the energy deviation (in cm^{-1}) corresponding to the scatter of $\Delta\nu_n$.

C. $^1\Pi_g$ and $^1\Delta_g$ symmetries

The eigenchannel quantum defects for $^1\Pi_g$ and $^1\Delta_g$symmetry exhibit a behavior similar to that displayed in Figs. 1(a)–1(d) and are not shown. Tables IV and V contain the computed $\nu_n(R)$ curves for $^1\Pi_g$ and $^1\Delta_g$ bound and resonance states, and Fig. 6 is the corresponding $\Delta\nu_n(R)$ plot for the bound states associated with these symmetries, while the upper part Fig. 4 contains the $\Delta\nu_n(R)$ values for the resonance positions of $^1\Pi_g$ and $^1\Delta_g$ symmetry. Table VI contains the calculated widths for the $^1\Pi_g$ and $^1\Delta_g$ resonances.

The *ab initio* quantum defect surfaces μ_α for $^1\Pi_g$ and $^1\Delta_g$ symmetry are remarkably smooth in both E and R. This is particularly true for the $^1\Delta_g$ quantum defects which are nearly flat and which we discuss first. The channel structure for the $^1\Delta_g$ symmetry for $\tilde{l}\leqslant 3$ is indeed itself very simple as it consists only of one single excited channel $1\tilde{s}\sigma\epsilon\tilde{d}\delta$ and

TABLE III. Widths (in rydbergs) for core excited $2\tilde{p}\sigma n\tilde{l}\sigma\ ^1\Sigma_g^+$ resonances of H_2. The orbital designations $nl\lambda$ are valid for small R only.

R	$2\tilde{p}\sigma$	$3\tilde{p}\sigma$	$4\tilde{p}\sigma$	$4\tilde{f}\sigma$
1.0	0.0225	0.0049	0.0018	1.7(−6)
1.2	0.0375	0.0068	0.0023	2.5(−6)
1.4	0.0491	0.0073	0.0034	
1.5	0.0476	0.0081	0.0033	6.2(−6)
1.6	0.0519	0.0093	0.0035	2.4(−5)
1.8	0.0674	0.0111	0.0042	
2.0	0.0834	0.0125	0.0047	5.5(−6)
2.2	0.1110	0.0130	0.0047	
2.4	0.1194	0.0129	0.0045	
2.5	0.1487	0.0120	0.0045	
2.6	0.0905	0.0113	0.0045	
3.0		0.0110	0.0046	4.6(−6)
3.5		0.0120	0.0055	4.0(−6)
4.0		0.0160	0.0075	5.6(−5)
4.5		0.0264	0.0098	0.000 22
5.0			0.0176	0.000 48

one doubly excited channel $2\tilde{p}\sigma\epsilon\tilde{f}\delta$. Both channels correspond to a nearly nonpenetrating outer electron and thus have small quantum defects and their coupling (off-diagonal quantum defect) is also small. Owing to the simple $^1\Delta_g$ channel structure and weak interchannel couplings, the potential energy and resonance curves run nearly perfectly parallel to the corresponding ion curves. The corresponding deviations $\nu_{ab\ initio} - \nu_{R\text{-matrix}}$ (upper part of Fig. 6) are smaller than those for $^1\Sigma_g^+$ symmetry. The $\nu_n(R)$ values of the $2\tilde{p}\sigma 4\tilde{f}\delta$ resonances (Table V) are almost integers. The lowest $^1\Delta_g$ resonance is so high that it does not cross the threshold in the R-range considered here, and no avoided crossings (which would be weak) occur in this range.

The $^1\Pi_g$ channel structure, potential curves, and resonance positions exhibit characeristics intermediate between those discussed for the $^1\Sigma_g^+$ and $^1\Delta_g$ symmetries. The channel structure for $\tilde{l} \leqslant 3$ consists of the single ground state core channel $1\tilde{s}\sigma\epsilon\tilde{d}\pi$ and two excited core channels $2\tilde{p}\sigma\epsilon\tilde{p}\pi$ and $2\tilde{p}\sigma\epsilon\tilde{f}\pi$. Below the threshold ($R > 3.5$) the continuation of the $2\tilde{p}\sigma 2\tilde{p}\pi$ resonance gives rise to avoided crossings and a potential maximum in the lowest bound state $3\tilde{d}\pi I$. The deviations $\Delta\nu_n = \nu_{ab\ initio} - \nu_{R\text{-matrix}}$ for the bound $^1\Pi_g$ states shown in Fig. 6 (lower part) are again comparable to those for the $^1\Sigma_g^+$ states albeit somewhat smoother. The deviations $\Delta\nu_n(R)$ of the present $^1\Pi_g$ resonance positions from those obtained by Tennyson [13] are shown in Fig. 4 (upper part). A striking feature in this plot is the large deviation, more than 0.2 on the quantum defect scale, of the resonance position $2\tilde{p}\sigma 2\tilde{p}\pi$ obtained here from that of Ref. [13] for $R = 3.5$. A similar but less pronounced deviation occurs for $2\tilde{p}\sigma 3\tilde{p}\pi$ at the same R value. We note that our corresponding $\nu_n(R)$ function (third column of Table V) is much smoother than that given in Ref. [13]. Evidence for the possible correctness of our resonance energy comes from Ref. [14] whose corresponding value yields the deviation indicated by a cross in Fig. 4 ($R = 3.5$) which, when substituted, leads to a decrease of the corresponding error bar and energy value on the right of Fig. 4 by a factor of 10. The widths of $2\tilde{p}\sigma n\tilde{p}\pi$ resonances (Table VI) are compared with the values from Ref. [13] in Fig. 5b. For $n \geqslant 4$ the $2\tilde{p}\sigma n\tilde{p}\pi$ and $2\tilde{p}\sigma n\tilde{f}\pi$ resonances occur as pairs, with the former characterized by a comparatively large width and the latter characterized by a much smaller width. We find that this pair of resonances overlaps increasingly with increasing R. This may be the reason why in Ref. [13] there is a sudden drop of the width Γ near $R = 2$ [Fig. 5(b)]. We suspect that the $2\tilde{p}\sigma 4\tilde{p}\pi$ resonance has been missed for $R > 2$ in the earlier calculations, and that the values given for this range in fact correspond to the much sharper $2\tilde{p}\sigma 4\tilde{f}\pi$ resonance (Fig. 7). In Ref. [14] both resonances have been found, and these authors indeed point out that an avoided crossing of the $2\tilde{p}\sigma 4\tilde{p}\pi$ and $2\tilde{p}\sigma 4\tilde{f}\pi$ configurations occurs near $R = 2.3$ a.u. We would like to add here that the continuum phase-shift sum from which we derive our widths and energies indicates that the resonances are overlapping so that strictly speaking the widths and positions become undefined in the crossing region. Thus the fact that we find the higher resonance to be sharper than the lower one for all R values considered, without exchange of character as found in Ref. [14], is not necessarily in contradiction with the statements made in the earlier work.

D. $\tilde{f}$ type resonances

The tables of Sánchez and Martin [14] provide the most recent and systematic survey of the $2\tilde{p}\sigma n\tilde{f}\lambda$ core excited resonances of $^1\Sigma_g^+$, $^1\Pi_g$, and $^1\Delta_g$ symmetry. Here we shall discuss the $n = 4$ members of these resonance Rydberg series.

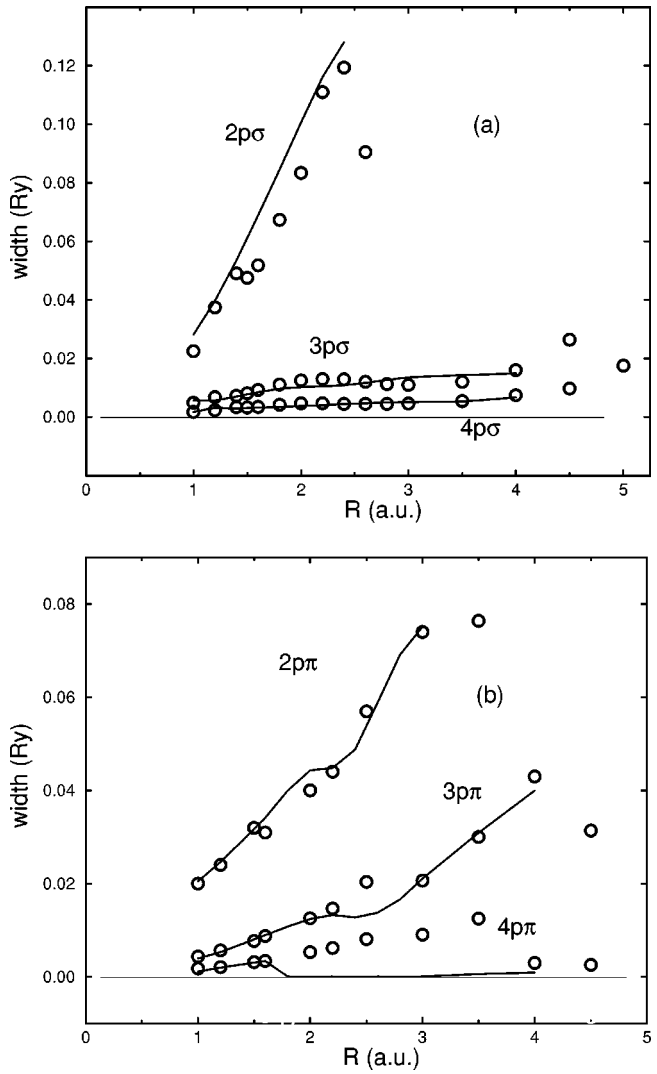

FIG. 5. Widths of (a) the $2\tilde{p}\sigma n\tilde{p}\sigma\ {}^1\Sigma_g^+$ and (b) the $2\tilde{p}\sigma n\tilde{p}\pi\ {}^1\Pi_g (n=2-4)$ resonances in H_2 as functions of internuclear distance. Reference [13], full lines; present work, circles.

Figure 7(a) presents the effective principal quantum number curves $\nu_{n=4}(R)$ derived from the resonance energies given in Ref. [14] (full lines), as well as our present results from Tables II and V (circles, squares, and diamonds). Surprisingly, the two sets of data show a markedly different behavior as functions of the internuclear distance. While the $\nu_{n=4}(R)$ curves from Ref. [14] rise steeply with R, our effective principal quantum numbers stay close to the integer value $n=4$ in agreement, for $\lambda=0$ and 2, with the calculations of Shimamura, Noble, and Burke [15] and Tennyson [13] (dashed lines in the figure). This latter behavior is in line with the expected behavior of a nearly nonpenetrating resonance electron. An additional surprising feature of the calculations of Ref. [14] is that the three λ components are calculated virtually degenerate, while our calculations predict a small but non-negligible λ structure for the same resonances.

Figure 7(b) illustrates the widths of these resonances. Again, owing to the weakly penetrating character of the $\tilde{l}=3$ electron, the coupling to the ion ground state continua is expected to be weak, with the result that according to our calculations the largest widths are two orders of magnitude smaller than those of the $2\tilde{p}\sigma n\tilde{p}\lambda$ resonances shown in Fig. 5. Indeed, for $R\leqslant 3$ our calculated widths are reduced by another two orders of magnitude, highlighting the almost strictly nonpenetrating character of the outer electron when R is small. The transition between the two electronic autoionization regimes takes place rather abruptly near $R=3.5$ a.u. This behavior is common to all λ components of the $\tilde{f}\lambda$ resonances. Figure 7(b) also contains the $\tilde{f}$ type resonance widths calculated previously (full lines, [14]; dashed lines, [13,15]). Although the overall trends are the same as we find, Fig. 7(b) shows that the values obtained previously are substantially larger than ours, in fact by as much as an order of magnitude for the largest R values.

IV. DISCUSSION

A. Ground state core and excited state core quantum defects

In spite of their rather simple appearance, the *ab initio* quantum defect surfaces such as those displayed in Fig. 1 contain a great deal of physical information in compact form concerning the interactions between the electrons and protons in highly excited H_2. We have illustrated this is the preceding section by extracting from them several physical parameters, such as potential energy curves of various shapes, as well as resonance position curves and widths.

TABLE IV. Clamped nuclei effective Rydberg principal quantum numbers $\nu_n(R)$[a] for bound ${}^1\Pi_g$ and ${}^1\Delta_g$ states of H_2. The orbital designations $nl\lambda$ are valid for small R only.

R	$3d\pi I$	$4d\pi R$	$5d\pi$	$6d\pi$	$3d\delta J$	$4d\delta S$	$5d\delta$	$6d\delta$
1.0	3.025	4.011	5.003	6.004	3.004	4.004	5.004	6.003
1.5	3.009	3.984	4.988	5.984	3.011	4.010	5.010	6.010
2.0	2.983	3.972	4.967	5.966	3.019	4.019	5.018	6.018
2.5	2.961	3.942	4.937	5.934	3.026	4.028	5.028	6.027
3.0	2.918	3.888	4.878	5.872	3.040	4.038	5.037	6.037
3.5	2.834	3.772	4.740	5.719	3.050	4.048	5.046	6.046
4.0	2.675	3.552	4.477	5.426	3.060	4.056	5.055	6.054
4.5	2.469	3.365	4.282	5.223	3.069	4.063	5.061	6.060
5.0	2.299	3.278	4.173	5.058	3.076	4.068	5.064	6.062

[a]Equation (3).

TABLE V. Clamped nuclei energies and effective Rydberg principal quantum numbers for core excited $2\tilde{p}\sigma n\tilde{l}\pi\ ^1\Pi_g$ and $2\tilde{p}\sigma n\tilde{l}\delta\ ^1\Delta_g$ resonances of H_2.

	$2\tilde{p}\pi$		$3\tilde{p}\pi$		$4\tilde{p}\pi$		$4\tilde{f}\pi$		$4\tilde{f}\delta$		$5\tilde{f}\delta$	
R	E[a]	ν[a]	E	ν	E	ν	E	ν	E	ν	E	ν
1.0	1.457	1.776	1.645	2.789	1.704	3.789	1.713	4.044	1.712	4.002	1.734	5.001
1.2	1.248	1.827	1.423	2.836	1.479	3.832	1.486	4.043				
1.5	0.973	1.895	1.133	2.902	1.186	3.897	1.191	4.048	1.189	4.002	1.212	5.002
1.6	0.892	1.914	1.047	2.919	1.099	3.915	1.104	4.048				
2.0	0.614	1.977	0.757	2.975	0.807	3.968	0.809	4.049	0.808	4.000	0.830	5.000
2.5	0.364	2.044	0.493	3.014	0.541	4.002	0.543	4.050	0.541	4.000	0.564	5.000
3.0	0.196	2.115	0.310	3.032	0.357	4.012	0.358	4.054	0.357	4.002	0.379	5.004
3.5	0.077	2.162	0.180	3.004	0.228	4.006	0.230	4.051	0.228	4.002		
4.0			0.088	2.973	0.139	4.017	0.139	4.020	0.139	4.007	0.161	5.010
4.5			0.023	2.950	0.074	3.931	0.076	4.019	0.076	4.009	0.098	5.011
5.0									0.032	4.011	0.055	5.017

[a]Cf. caption for Table II.

Here, we shall briefly discuss yet another aspect, namely the relationship between the effective principal quantum numbers of bound states and the analogous quantities of core excited resonances.

Figure 8 depicts the evolution with internuclear distance of the quantum defect of the $3\tilde{p}\lambda$ electron with $\lambda=0$ and 1 moving in the field of either the $1\tilde{s}\sigma$ ground state core of the $2\tilde{p}\sigma$ excited state core. These R-dependent effective Coulombic quantum defects are defined by $\mu(R)=n-\nu_n(R)$, where $\nu_n(R)$ is given by Eq. (3). By their definition they are one-electron quantities, but they are effective because $U_n(R)$ in Eq. (3) contains the effects of configuration interaction. The curves labeled $1\tilde{p}\sigma 3\tilde{p}\sigma$ and $1\tilde{s}\sigma 3\tilde{p}\pi$ (full symbols) are ground state core quantum defects and correspond to the $B'^1\Sigma_u^+$ and $D^1\Pi_u$ bound states of H_2, respectively; the corresponding data have been taken from Ref. [1]. The curves labeled $2\tilde{s}\sigma 3\tilde{p}\sigma$ and $2\tilde{s}\sigma 3\tilde{p}\pi$ (empty symbols) are excited core quantum defects corresponding to the $^1\Sigma_g^+$ and $^1\Pi_g$ resonant states from Tables II and IV. The data points for $R=0$ (united atom He) are drawn assuming that the ground state core quantum defects correlate with $1s3p\ ^1P^o$, while the excited core quantum defects correlate with the $2,3a\ ^1D^o$ atomic resonance calculated by Conneely and Lipsky [25].

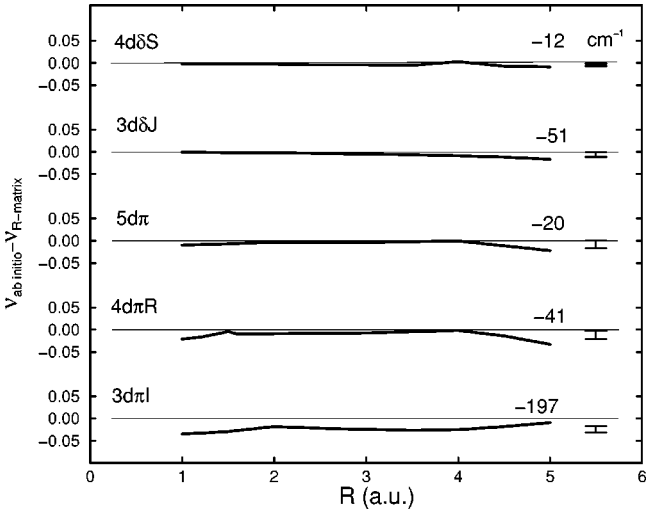

FIG. 6. Deviations $\Delta\nu_n=\nu_{ab\ initio}-\nu_{R\text{-matrix}}$ as functions of R for the bound $1-3\ ^1\Pi_g$ and $1\text{-}2\ ^1\Delta_g$ states. *Ab initio* data from Refs. [3] and [4] except for the $3\ ^1\Pi_g(5d\pi)$ state where they are from Ref. [6] (cf. caption for Fig. 3).

The ground state core quantum defects exhibit the well-known behavior of the promoted antibonding $3\tilde{p}\sigma$ electron and the unpromoted nonbonding $3\tilde{p}\pi$ electron discussed in the past many times, e.g., in Refs. [26–28]. The quantum defect of the $^1\Sigma_u^+$ component exhibits a characteristic strong increase with R, approaching unity at large R, while that of the $^1\Pi_u$ component is much less R dependent and remains small throughout the R range shown. The excited core quantum defects provide analogous scattering information pertaining to a p electron impinging on the core in a different state. We see that the quantum defects are larger (more posi-

TABLE VI. Widths (in rydbergs) for core excited $2\tilde{p}\sigma n\tilde{l}\pi\ ^1\Pi_g$ and $2\tilde{p}\sigma n\tilde{l}\delta\ ^1\Delta_g$ resonances of H_2. The orbital designations $nl\lambda$ are valid for small R only.

R	$2\tilde{p}\pi$	$3\tilde{p}\pi$	$4\tilde{p}\pi$	$4\tilde{f}\pi$	$4\tilde{f}\delta$
1.0	0.0200	0.0044	0.0018	3.0(−6)	3.4(−6)
1.2	0.0240	0.0057	0.0021	5.2(−6)	
1.5	0.0320	0.0077	0.0032		6.0(−7)
1.6	0.0310	0.0088	0.0034	4.6(−6)	
2.0	0.0400	0.0126	0.0053	3.0(−6)	4.9(−6)
2.2	0.0440	0.0147	0.0062		
2.5	0.0570	0.0204	0.0081	6.4(−6)	9.0(−6)
3.0	0.0740	0.0207	0.0091	9.8(−5)	6.0(−7)
3.5	0.0764	0.0300	0.0125	8.6(−5)	2.2(−6)
4.0		0.0430	0.0030	0.000 18	0.000 14
4.5		0.0314	0.0026	0.000 17	0.000 42
5.0					0.000 86

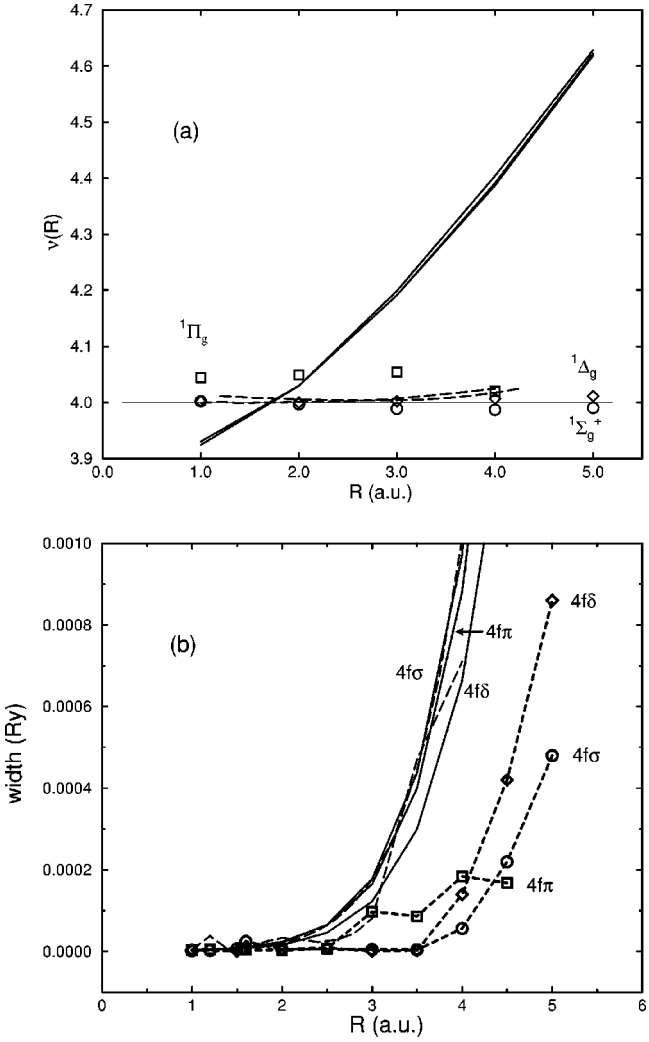

FIG. 7. (a) Effective principal quantum numbers $\nu_n(R)$, (b) widths, of the $2\tilde{p}\sigma 4\tilde{f}\lambda$ resonances. Full lines, Ref. [14]; long dashed lines, Refs. [15] ($4\tilde{f}\sigma$) and [13] ($4\tilde{f}\delta$). Present work: symbols [connected by dotted lines in (b)]: circles ($4\tilde{f}\sigma$), squares ($4\tilde{f}\pi$), and diamonds ($4\tilde{f}\delta$).

tive) as should be expected because the core region is increased and, in particular, the $2\tilde{p}\sigma$ core electron is a precursor of the $3\tilde{p}\sigma$ scattered electron. Thus the effect of core penetration is enhanced. The antibonding versus nonbonding behavior of the quantum defect curves as functions of R however is again clearly visible. At the same time we also see the limits of this one-electron interpretation of quantum defects: for $R \approx 4$, the $^1\Sigma_g^+$ excited core quantum defect compoent starts bending down towards smaller values. This effect is due to configuration interaction: the $3\tilde{p}\sigma$ resonance comes down in energy as R increases and begins to interact with the lower lying bound states of the same symmetry which push the resonance to higher energy and thus decrease its quantum defect. The opposite effect pushes the bound state quantum defects up as R increases as has been shown in Ref. [1]. Indeed, part of the strong increase of the $1\tilde{s}\sigma 3\tilde{p}\sigma$ curve in Fig. 8 is due to configuration interaction and should not be explained in tems of a pure one-electron Rydberg

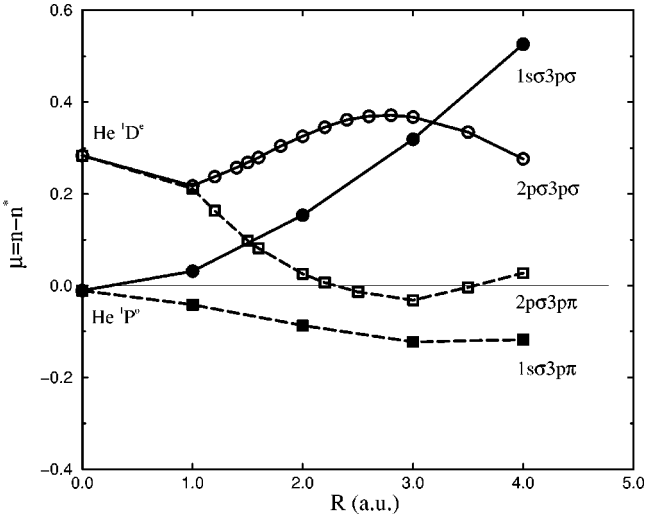

FIG. 8. Ground state core and excited state core effective quantum defects $\mu_n(R)=n-\nu_n(R)$ [Eq. (3)] as functions of R for $n=3,\tilde{l}=1$. Filled symbols, ground state core quantum defects (*ungerade* symmetry); empty symbols, excited core quantum defects (*gerade* symmetry). Circles, $^1\Sigma$ symmetry; squares, $^1\Pi$ symmetry.

image. The $^1\Pi_g$ resonance lies higher and crosses the ground state ion curve at larger R. As a consequence the decrease of the quantum defect is not visible in Fig. 8.

Plots similar to Fig. 8 may be drawn also for the $3\tilde{s}\sigma$ and $3\tilde{d}\lambda$ electrons as well as for principal quantum numbers $n \neq 3$. The separation of ground state quantum defects (to higher values) and of excited state quantum defects (to lower values) with increasing R is a common feature of all these plots, related to the fact that the $1\tilde{s}\sigma$ and $2\tilde{p}\sigma$ core states coalesce as $R \to \infty$.

B. Transformation to spherical coordinates and quantum defects

In Refs. [16,17] nondiagonal quantum defect matrices were derived from the quantum chemical potential energy curves of Refs. [2,3] and [4]. These earlier quantum defects matrices have been used successfully in rovibronic level calculations of the mixed *gerade* excited state structures [18], and they have also served for the calculation of the ionization/dissociation dynamics of H_2 excited from the $EF^1\Sigma_g^+$ double minimum state [30] as well as for the prediction of wavepacket dynamics in highly excited ionizing and dissociating *gerade* H_2 [31]. As Greene and Yoo [20] pointed out, the relationship between such quantum defect matrices obtained *indirectly* from potential energy curve data and those calculated *directly* in an *ab initio* R-matrix procedure such as utilized here, is not obvious and is more complex than in atomic problems, because it depends on the number of channels explicitly included, and is complicated by the fact that some of the channels (e.g., $2\tilde{p}\sigma_u \epsilon \tilde{p}\sigma_u$; cf. Fig. 2) are strongly closed at small internuclear distances while they become weakly closed (in the sense of MQDT) at larger R values.

In Refs. [16] and [17] the multichannel quantum defect secular Eq. (2) was used and the K-matrix elements $K_{kk'}$

adjusted in such a way that the solutions $U_n(R)$ fit the quantum chemical potential energy curves as best as possible. This goal was achieved in Refs. [16] and [17] with almost spectroscopic accuracy, although a number of *ad hoc* assumptions also had to the made (e.g., the neglect of most of the energy dependencies and of some of the R dependencies). In the earlier work however spherical coordinates were used instead of the spheroidal coordinates used here, and the accumulated channel phases β_k were taken to be one-center Coulombic rather than two-center Coulombic. Thus for the purpose of a detailed comparison we must make a transformation to a spherical representation and replace the numerical channel functions used in the external zone by the appropriate analytic regular and irregular Coulomb functions used in Ref. [17].

We return at this point to the R-matrix solutions Ψ_β of Eq. (10) of Ref. [1] and their spheroidal asymptotic form Eq. (16) of Ref. [1]:

$$\Psi_\beta(E,\omega,\xi) = \sum_k \Phi_k(E,\omega) \frac{1}{\sqrt{\xi^2-1}} \times [f_k(\epsilon_c,\xi) I_{k\beta} - g_k(\epsilon_c,\xi) J_{k\beta}], \quad (5)$$

where Φ_k contains the core wave function of channel k as well as the angular factor of the outer electron. ω thus denotes all coordinates except ξ. The matrices I and J consist of matching coefficients which yield the desired spheroidal reaction matrix $K=JI^{-1}$. Equation (5) is valid for any $\xi \geqslant \xi_0$ with the coefficients $I_{k\beta}$ and $J_{k\beta}$ determined for $\xi=\xi_0$. We now use Eq. (5) to evaluate the R-matrix eigensolutions on a sphere $r=r_0$, centered on the midpoint between the nuclei. Then the matching procedure, Eqs. (19)–(22) of Ref. [1], is repeated with the difference that the asymptotic channel functions in the summation of Eq. (5) are now

$$\Psi_\beta(E,\omega,r) = \sum_k \phi_c(\xi_1,\eta_1,\varphi_1) Y_{1\lambda}(\theta,\phi) \frac{1}{r} \times [f_k^{(sph)}(\epsilon_c,r) I_{k\beta}^{(sph)} - g_k^{(sph)}(\epsilon_c,r) J_{k\beta}^{(sph)}], \quad (6)$$

where ϕ_c is the core wavefunction, Y are ordinary spherical harmonics, and $f_k^{(sph)}$ and $g_k^{(sph)}$ are the radial Coulomb functions originally introduced by Ham [32] (see Seaton [21], his nearly analytic functions f and h). The relation

$$K_{kk'}^{(sph)} \equiv \tan \pi\eta_{kk'} = \sum_\beta J_{k\beta}^{(sph)} I_{k'\beta}^{(sph)-1} \quad (7)$$

now yields *spherical* quantum defect matrices $\eta_{kk'}$, so-called η defects in the terminology of Ham [32], which are appropriate for use in the framework of the customary quantum defect/frame transformation theory. (Our $\mathbf{K}^{(sph)}$ corrsponds to $\mathbf{Y}$ in Seaton's notation.)

In order to be consistent with the present spheroidal R-matrix calculations and with the work of Refs. [16] and [17] where the $(2\tilde{p}\sigma)^2$ resonance is treated as the lowest member of a Rydberg channel, we have taken the sphere $r=r_0$ just slightly larger than the large axis of the ellipsoid $\xi=\xi_0$, typically $r_0=(R/2)\xi_0+\frac{1}{2}$. We have ascertained that the η defects thus determined yield bound state $\nu_n(R)$ values very close to those listed in Table I. The resulting spherical $^1\Sigma_g^+$ η defects are shown in Fig. 9 for the range $2 \leqslant R \leqslant 5$ a.u. and for an energy of 0.1 Ry below the $1\tilde{s}\sigma$ H_2^+ threshold corresponding to $\nu \approx 3.2$ which is in the middle of the range for which the η matrices of Ref. [17] were derived.

In Refs. [16–18] only the channels $1\tilde{s}\sigma\epsilon s\sigma$, $1\tilde{s}\sigma\epsilon d\sigma$, and $2\tilde{p}\sigma\epsilon p\sigma$ (in short-hand notation: s,d, and p) were considered, while $2\tilde{p}\sigma\epsilon f\sigma$ (short-hand f) was excluded. Figure 9(a) illustrates the $lf(1=0-3)$ spherical $^1\Sigma_g^+$ η quantum defect functions obtained here. Two elements, df and ff, are seen to become as large as 0.3 near $R=5$, indicating that the neglect of the f excited core channel in Refs. [16–18] was not justified because the single-center representation of the nonpenetrating $\tilde{f}$ wave becomes inappropriate for $R \geqslant 2.5$. Note that by contrast in the spheroidal formulation all quantum defect elements involving an $\epsilon\tilde{f}\lambda$ outer electron are smaller than 0.03 (see Fig. 1, for example) throughout the energy and R ranges considered in this work.

We next compare in Fig. 9(b) the diagonal η elements ss, dd, and pp (short-hand notation, represented by circles connected by dashed lines) with those illustrated in Ref. [18] (full lines in Fig. 9). The crucial region of R values for the interactions between singly and doubly excited configurations of $^1\Sigma_g^+$ symmetry is between $R=2$ (minimum of H_2^+ $1\tilde{s}\sigma$) and $R=3$ [crossing of $(2\tilde{p}\sigma)^2$ with the singly excited Rydberg manifold]. Figure 9(b) shows that in this R range the previous and present η defects are indeed quite close to each other, with deviations of the order of ≈ 0.05. This may be considered as a good agreement. Outside the $R=2-3$ range however the two sets of quantum defect functions diverge substantially from one another, no doubt because of the various simplifying assumptions which had to be made in the earlier work. Nevertheless, it is probably, fair to say, with a dose of optimism, that the overall R dependencies are qualitatively similar (e.g., the overall decrease of pp for $R \geqslant 3$, or the negative values of dd in the intermediate range followed by a strong increase up to large positive values).

Figure 9(c) finally illustrates the off-diagonal sd, sp, and dp quantum defects. We see, again, that in the crossing region ($R \approx 3$) the two sets of quantum defects agree rather closely, with the dp interaction larger than sp, and sd small with opposite sign. Again, however, the R dependencies anticipated in the earlier work are not corroborated by the present R-matrix results.

V. CONCLUSION

The main result of this work is a set of quantum defect matrices for all singlet gerade symmetry channels of H_2 with $1 \leqslant 3$ and $\lambda \leqslant 2$ that are smooth functions of both energy and internuclear distance. We have seen that these eigenchannel surfaces fall into two rather distinct classes, a few that are active and exhibit a significant evolution as function of R and E, and all those that are inactive and are near zero throughout the E, R ranges studied here. As stated earlier, this double smoothness should prove helpful when, as planned, a purely *ab initio* description of H_2 fragmentation dynamics is imple-

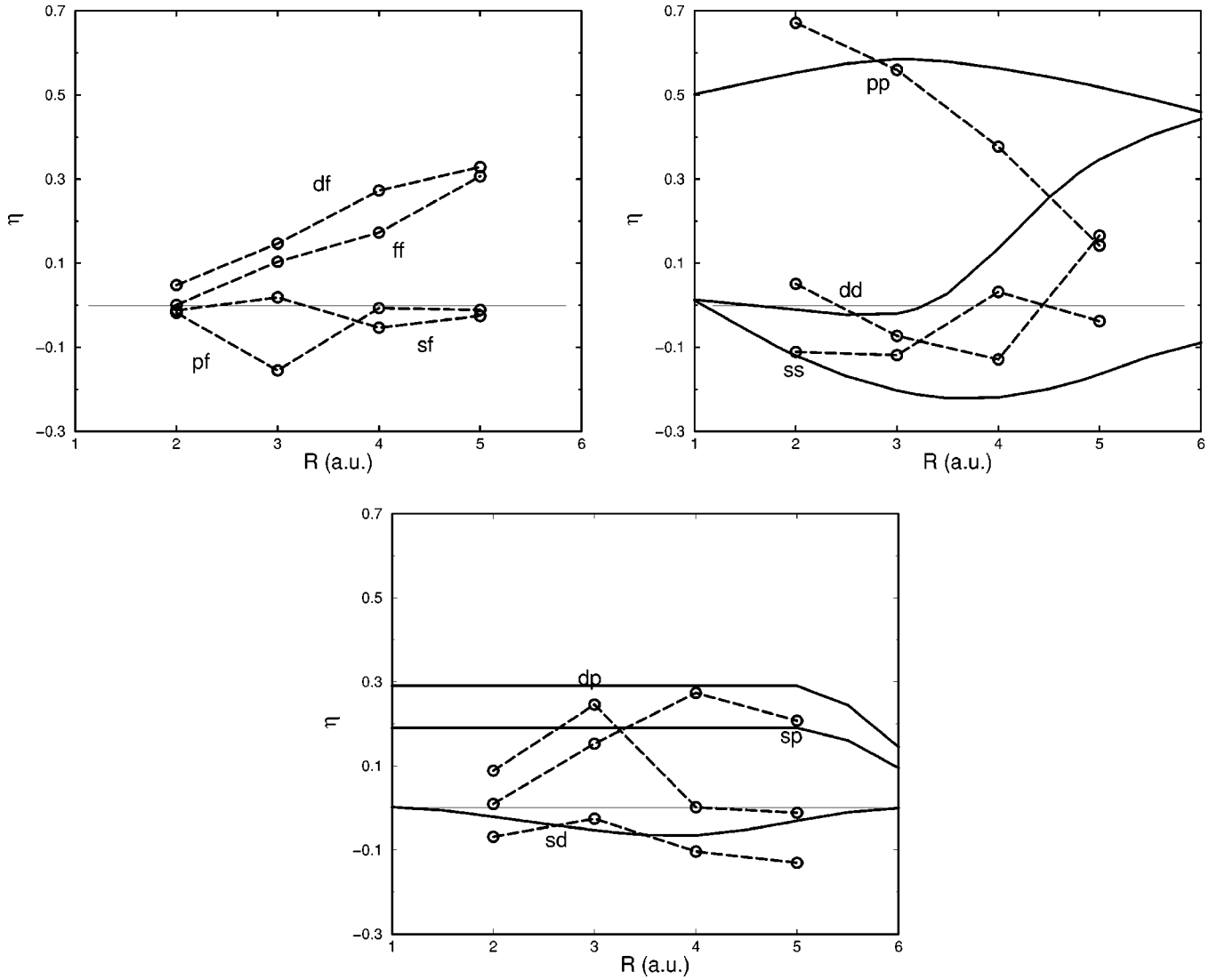

FIG. 9. Spherical η defects for $^1\Sigma_g^+$ symmetry. Circles connected by dashed lines: present R-matrix results. Full lines: values from Ref. [18]. l denotes the orbital angular momentum of the outer electron with the core in the ground state for *even* l, and with the core in the excited state for *odd* l, respectively: (a) diagonal and off-diagonal elements involving $l=3$; (b) diagonal elements for $l\leqslant 2$; (c) off-diagonal elements for $l,l'\leqslant 2$. For clarity, the labels in (b) and (c) are placed near the R values where the corresponding dashed and full lines cross or come closest.

mented. Interpolation procedures will be used to obtain the quantum defect matrices on energy and internuclear grids as desired. These interpolation procedures can be applied directly to the quantum defect matrices themselves irrespective of the dimensions of the variational basis sets used in the calculation for a given R. This possibility has not been fully exploited in the present work since we have taken essentially the same basis set for all R values. If required, however, the convergence can be improved locally, e.g., at large R, a possibility which is not offered in the approach of Yoo and Greene [20] which requires a single basis for the full R range considered.

We have tested the accuracy of the R-matrix quantum defects by using them in the framework of generalized quantum defect theory to calculate clamped-nuclei potential energy curves $U_n(R)$ for $n=2-5$, and comparing these with highly accurate state-of-the-art quantum chemical *ab initio* potential energy curves. The effective principal quantum numbers (modulo 1), equivalent to the R-dependent electron-ion effective phase shift, are found to be correct to within about 2% which we consider satisfactory agreement. Salient features, such as the double-minimum or shelf structures of some of the states, are reproduced correctly. We have also used the R-matrix quantum defects to calculate electronic autoionization resonance positions and widths which have again been compared with previous first principles scattering calculations. Our $\tilde{p}$ resonances agree well with the previous calculations (with a single exception, cf. Fig. 4). No such general consensus has been reached yet with regard to the more elusive $\tilde{f}$ type resonances for which diagreement persists between our and previous work, but also between various earlier studies.

The lowest $^1\Sigma_g^+$ doubly excited configuration $(2\tilde{p}\sigma)^2$ produces the low-lying outer well in the EF state near R

≈ 4.5 a.u. (see Fig. 2). This state is usually considered to be a valence rather than a Rydberg state, indeed it turns into the $H^+ + H^-$ ionic configuration for R values between 5 and 7 a.u. It is thus interesting to note that our R- matrix calculations yield this state as the lowest member of the $2\tilde{p}\sigma n\tilde{p}\sigma$ resonance Rydberg series with hardly any trace of resonant behavior visible in the quantum defects μ_α themselves at the corresponding energy (Fig. 1). By contrast, the recent Wigner-Eisenbud R- matrix calculations of Hiyama and Child [29] of the NO molecule yielded the valence states of that molecule in the form of poles of the **K** matrix, which disrupt the otherwise smooth evolution of its elements with energy and internuclear distance. Our calculations differ from those of Ref. [29] in that we use spheroidal rather than spherical coordinates, and therefore are able to reduce the reaction volume considerably (by about a factor of two) as a consequence of a more realistic description of the asymptotic field outside the core, two half-charges separated by R rather than a unit point charge (the "halfium" description in the terminology of Ref. [1]). The wavefunction of the $(2\tilde{p}\sigma)^2$ configuration therefore spills out into the asymptotic zone and thereby becomes amenable to a Rydberg description. Another advantage of the halfium description is the fact that the $\tilde{l}=3$ partial wave remains nonpenetrating throughout the R range studied here and hence participates only little in the channel interactions. In the spherical Coulomb description on the other hand, the $l=3$ wave undergoes strong l mixing for $R \geqslant 3$ as shown by the large off-diagonal quantum defect elements displayed in Fig. 9(a).

It has been possible in the present work to make a direct comparison of directly calculated R-matrix quantum defect matrices with the spherical Ham η quantum defect matrices derived previously in Refs. [16] and [17] on the basis of the lowest quantum chemical *ab initio* potential energy curves. This comparison is important in view of the fact that the matrices published in 1994 constitute the only available set of dynamical parameters (which in a sense is *ab initio*), which when combined with rovibronic multichannel quantum defect theory, is capable to yield a realistic description of the various continuum processes occurring near the ionization and dissociation thresholds of H_2. The comparison, made in Figs. 9(b) and 9(c), reveals substantial shortcomings of the previous approach, but at the same time many of the crucial details turn out to be in almost quantitative agreement.

ACKNOWLEDGMENTS

This project has been supported in part within the framework of a DGRST/CNRS Tunisian-French cooperation. We thank Professor Z. Ben-Lakhdar (Tunis) for her unfailing enthusiastic support over several years. S. B. acknowledges the hospitality of the Université de Paris-Sud and the Laboratoire Aimé Cotton during repeated stays at Orsay within the framework of her thesis work carried out jointly at the Faculty of Sciences of Tunis and at the Université de Paris–Sud (Orsay). Dr. E. Reinhold (Amsterdam) and Dr. M. Aymar (Orsay) are thanked for their help with the evaluation of the Ham-type Coulomb functions.

[1] M. Telmini and Ch. Jungen, Phys. Rev. A **68**, 062704 (2003).
[2] L. Wolniewicz and K. Dressler, J. Chem. Phys. **100**, 444 (1994).
[3] L. Wolniewicz, J. Mol. Spectrosc. **169**, 329 (1995).
[4] L. Wolniewicz, J. Mol. Spectrosc. **174**, 132 (1995).
[5] T. Detmer, P. Schmelcher, and L. S. Cederbaum, J. Chem. Phys. **109**, 9694 (1998).
[6] A. Spielfiedel, J. Mol. Spectrosc. **217**, 162 (2003).
[7] T. F. O'Malley, J. Chem. Phys. **51**, 322 (1969).
[8] C. Bottcher and K. Docken, J. Phys. B **7**, L5 (1974).
[9] H. Takagi and H. Nakamura, J. Phys. B **13**, 2619 (1980).
[10] L. A. Collins and B. I. Schneider, Phys. Rev. A **27**, 101 (1983).
[11] S. L. Guberman, J. Chem. Phys. **78**, 1404 (1983).
[12] J. Tennyson, C. J. Noble, and S. Salvini, J. Phys. B **17**, 905 (1984).
[13] J. Tennyson, At. Data Nucl. Data Tables **64**, 253 (1996).
[14] I. Sánchez and F. Martin, J. Chem. Phys. **106**, 7720 (1997).
[15] I. Shimamura, C. J. Noble, and P. G. Burke, Phys. Rev. A **41**, 3545 (1990).
[16] S. Ross and Ch. Jungen, Phys. Rev. Lett. **59**, 1297 (1987).
[17] S. C. Ross and Ch. Jungen, Phys. Rev. A **49**, 4353 (1994).
[18] S. C. Ross and Ch. Jungen, Phys. Rev. A **50**, 4618 (1994).
[19] B. Yoo, Ph.D. thesis, Louisiana State University, Baton Rouge, LA, USA, 1990.
[20] C. H. Greene and B. Yoo, J. Phys. Chem. **99**, 1771 (1995).
[21] M. J. Seaton, Rep. Prog. Phys. **46**, 167 (1983) (reprinted in Ref. [22]).
[22] *Molecular Applications of Quantum Defect Theory*, edited by Ch. Jungen (Institute of Physics, Bristol, 1996).
[23] C. H. Greene and Ch. Jungen, Adv. At. Mol. Phys. **21**, 51 (1985).
[24] Ch. Jungen and F. Texier, J. Phys. B **33**, 2495 (2000).
[25] M. J. Conneely and L. Lipsky, J. Phys. B **11**, 4135 (1978).
[26] R. S. Mulliken, J. Am. Chem. Soc. **88**, 1849 (1966).
[27] R. S. Mulliken, J. Am. Chem. Soc. **91**, 4615 (1969).
[28] G. Herzberg and Ch. Jungen, J. Mol. Spectrosc. **41**, 425 (1972).
[29] M. Hiyama and M. S. Child, J. Phys. B **35**, 1337 (2002).
[30] Ch. Jungen, S. T. Pratt, and S. C. Ross, J. Phys. Chem. **99**, 1700 (1995).
[31] F. Texier and Ch. Jungen, Phys. Rev. Lett. **81**, 4329 (1998).
[32] F. S. Ham, Solid State Phys. **1**, 127 (1955), reprinted in Ref. [22]).